Aerospace Science and Technology 127 (2022) 107679

Contents lists available at ScienceDirect

Aerospace Science and Technology

www.elsevier.com/locate/aescte

Large Eddy Simulation of optimal Synthetic Jet Actuation on a SD7003 airfoil in post-stall conditions

N.M. Tousi [a], J.M. Bergadà [a], F. Mellibovsky [b,*]

[a] *Department of Fluid Mechanics, Universitat Politècnica de Catalunya, Barcelona, 08034, Spain*
[b] *Department of Physics, Aerospace Engineering Division, Universitat Politècnica de Catalunya, Barcelona, 08034, Spain*

ARTICLE INFO

Article history:
Received 1 December 2021
Received in revised form 27 May 2022
Accepted 1 June 2022
Available online 10 June 2022
Communicated by Cummings Russell

Keywords:
Active Flow Control
LES/RANS
Optimisation
Aerodynamic efficiency
Flow structure

ABSTRACT

Aerodynamic performances may be optimised by the appropriate tuning of Active Flow Control (AFC) parameters. For the first time, we couple Genetic Algorithms (GA) with an unsteady Reynolds-Averaged Navier-Stokes (RANS) solver using the Spalart-Allmaras (SA) turbulence model to maximise lift and aerodynamic efficiency of an airfoil in stall conditions [1], and then validate the resulting set of optimal Synthetic Jet Actuator (SJA) parameters against well-resolved three-dimensional Large Eddy Simulation (LES). The airfoil considered is the SD7003, at the Reynolds number $Re = 6 \times 10^4$ and the post-stall angle of attack $\alpha = 14°$. We find that, although SA-RANS is not quite as accurate as LES, it can still predict macroscopic aggregates such as lift and drag coefficients, provided the free-stream turbulence is prescribed to reasonable values. The sensitivity to free-stream turbulence is found to be particularly critical for SJA cases. Baseline LES simulation agrees well with literature results, while RANS-SA would seem to remain a valid model to a certain degree. For optimally actuated cases, our LES simulation predicts far better performances than obtained by suboptimal SJA LES computations as reported by other authors [2] for the same airfoil, Re and α, which illustrates the applicability and effectiveness of the SJA optimisation technique applied, despite using the less accurate yet computationally faster SA-RANS. The flow topology and wake dynamics of baseline and SJA cases are thoroughly compared to elucidate the mechanism whereby aerodynamic performances are enhanced.

1. Introduction

Active Flow Control (AFC) may be applied to airfoils and wings to suppress or postpone flow separation thereby improving aerodynamic performance. One of the main advantages of AFC as compared to passive flow control is that no drag penalty is incurred in off-design conditions. AFC techniques usually fall in one of three different categories [3], namely moving body, plasma and fluidic actuation. Moving body actuators act on the geometry of the body to inject momentum into the flow [4]. Plasma actuators generate fast temporal response jets of ionised fluid by applying large electric potential differences [5–9]. Fluidic actuators (FA), which are by far the most common, inject/suck fluid to/from the boundary layer.

Among fluidic actuators, Synthetic Jet Actuators (SJA, sometimes also called Zero Net Mass Flow Actuators ZNMFA) are of particular interest because of their simplicity and demonstrated capability of suppressing flow separation [10–14]. For instance, SJAs have been shown more effective than Continuous Jet Actuators (CJA) at comparable power input levels in improving the performances of a stator compressor cascade [15–19]. SJAs do not require an external fluid supply, since their zero net mass flux can be simply obtained with an oscillating membrane (or reciprocating piston) housed inside a tiny cavity just beneath the surface. The back and forth displacement of the membrane alternatively sucks low momentum fluid from the near-wall and injects the fluid back with increased momentum.

A large number of numerical and experimental studies involving SJA implementation on airfoils has been published over the last couple of decades. Most of the research focuses on assessing the combined effect of two SJA parameters, namely the actuation frequency f_j and the jet momentum coefficient C_μ. The former is nondimensionalised with the airfoil chord C and the free-stream velocity U_∞ following $f_j/(U_\infty/C)$, while the momentum coefficient is defined as $C_\mu = (\rho_j U_j^2 h_j \sin\theta_j)/(\rho_\infty U_\infty^2 C)$, with h_j the jet width, ρ_j and ρ_∞ the jet and far field fluid densities, respectively, U_j the maximum jet velocity and θ_j the jet inclination angle with respect to the surface.

One of the first experimental studies looking into the effect on flow separation over an unconventional symmetric airfoil of the momentum coefficient, frequency and position of a synthetic

---

* Corresponding author.
E-mail address: fernando.mellibovsky@upc.edu (F. Mellibovsky).

https://doi.org/10.1016/j.ast.2022.107679

jet actuator was undertaken by Amitay et al. [19], Amitay and Glezer [20]. They found that placing the actuator close to the boundary layer separation point minimised the momentum coefficient required for flow reattachment. Actuating with frequencies of the same order of magnitude as the natural von Kármán vortex-shedding frequency ($f_j \sim f_{\mathrm{vK}} \simeq 0.7 U_\infty/C$) produced unsteady reattachment, while full flow reattachment could be obtained by actuating at about ten times the vortex-shedding frequency ($f_j/f_{\mathrm{vK}} \sim \mathcal{O}(10)$).

The effect of SJA on a NACA0015 airfoil at $Re = 8.96 \times 10^5$ was studied experimentally by Gilarranz et al. [21] and numerically (using LES) by You and Moin [22]. In the experiments, while actuation was rather ineffective below $\alpha \leq 10$, its effectiveness was seen to largely improve at higher values of α, managing to push the stall angle of attack from $\alpha_s = 12°$ to $18°$. At $\alpha > 25°$ the required actuation frequencies needed to obtain high lift coefficients were particularly large. Numerical simulations produced a 70% lift increase for SJA AFC parameters $C_\mu = 0.0123$, $f_j = 1.284 U_\infty/C$ and $\theta_j = 30.2°$ with respect to baseline. The same airfoil was experimentally analysed by Tuck and Soria [23] at the lower $Re = 3.9 \times 10^4$, and then simulated numerically via LES [24]. Maximum efficiency was obtained for SJA frequencies $f_j = 0.65 U_\infty/C$ and 1.3 in the experiments, intermediate values being not quite so effective. The combination of $C_\mu = 0.0123$ momentum coefficient with the highest frequency delayed stall from $\alpha_s = 10°$ for baseline to $18°$. The numerical simulations revealed that the optimal frequencies coincided with the baseline shedding frequency (f_{vK}) and its first harmonic ($2 f_{\mathrm{vK}}$). The same particulars were observed again by Buchmann et al. [25] in their high-repetition-rate PIV experiments. Itsariyapinyo and Sharma [26] revisited the same airfoil at $Re = 1.1 \times 10^5$ with LES simulations of SJA acting tangentially to the surface precisely at the trailing edge. The lift coefficient was seen to increase linearly when raising the momentum coefficient up to a certain threshold, beyond which point further improvement slowed down and saturated.

Kim and Kim [27] applied flow separation control to a NACA23012 airfoil at $Re = 2.19 \times 10^6$ and $\alpha \in [6°, 22°]$ in 5 different slat/flap/jet configurations using the Reynolds-averaged Navier-Stokes (RANS) equations and the k-ω SST turbulence model. Low actuation frequencies were found the most adequate to the reduction of the large separated regions, while the jet momentum coefficients required were large. They proposed the implementation of multi-array/multi-location SJA to reduce the required jet velocity, a solution that was successful. The same airfoil and Reynolds number were addressed by Monir et al. [28] in two different configurations using RANS and the Spalart-Allmaras turbulence model. They found that while SJA actuation at $\theta_j = 43°$ could improve aerodynamic efficiency substantially, tangential actuation was by far the optimum.

Experimental studies to evaluate the effects of SJA on separation control and wake topology on a NACA0025 airfoil at $Re = 10^5$ and $\alpha = 5°$ were undertaken by Goodfellow et al. [29]. They noticed that momentum coefficient was the primary control parameter, and obtained up to 50% drag decrease with C_μ above a certain threshold. The same airfoil at the same Reynolds number was analysed by Feero et al. [30], but at the higher $\alpha = 10°$. They reported that momentum coefficients required for flow reattachment were one order of magnitude lower for excitation frequencies about the vortex shedding frequency than for high frequencies. In a later study they considered the effects of jet location at the still larger $\alpha = 12°$ [31]. Flow control was all the more effective by locating the jet slot in the vicinity of the natural separation point. Zhang and Samtaney [32] investigated the dependence of SJA efficacy on excitation frequency for a NACA0018 airfoil at $\alpha = 10°$ and ultralow $Re = 1000$ using three-dimensional Direct Numerical Simulation (DNS). Three different frequencies were assessed ($f_j = 0.5 U_\infty/C$, 1 and 4) and, although aerodynamic performances improved in all cases, $f_j = 1 U_\infty/C$ was found the optimal.

As an airfoil specifically designed for low Reynolds number applications, the Selig-Donovan 7003 (SD7003) [33,34] has been recently investigated at $Re = 6 \times 10^4$ employing LES [35,36,2]. Breuer [35] tested several inlet turbulence intensities, ranging from nil to $Tu = 11\%$, at $\alpha = 4°$ with the object of understanding its impact on the Laminar Separation Bubble (LSB). He concluded that high Tu values managed to reduce and even suppress the LSB, thereby enhancing aerodynamic performance. Freestream unsteadiness effects were also assessed by Qin et al. [36], this time by exploring different inlet velocity oscillation amplitudes and frequencies, at the same $\alpha = 4°$. Flow separation was delayed and even suppressed during the acceleration phase, while the separation point progressed upstream towards the leading edge in the deceleration phase. Rodriguez et al. [2] applied SJA AFC to the SD7003 in their LES simulations at $\alpha = \{4°, 11°, 14°\}$ and obtained an aerodynamic efficiency increase of up to $\Delta\eta/\eta = 124\%$ at the highest α, actuation being less effective at pre-stall angles of attack.

All research on SJA AFC application to airfoils discussed so far was limited to straightforward parametric explorations merely intended to elucidate the separate effects of the various actuation parameters on aerodynamic performance. There exist, however, a number of studies aiming at systematic optimisation. Duvigneau and Visonneau [37] optimised SJA non-dimensional frequency, velocity amplitude and injection angle on a NACA0015 airfoil at $Re = 8.96 \times 10^5$ and for a range of $\alpha \in [12°, 24°]$. To do so, they coupled their flow solver with an optimisation algorithm first developed by Torczon [38]. An optimum choice of the three SJA parameters produced a lift increase of 34% and a stall angle delay from $\alpha_s = 19°$ to $22°$. A study of SJA on a NACA0012 airfoil at $Re = 2 \times 10^6$ and $\alpha = \{18°, 20°\}$ followed shortly after that employed a derivative-free algorithm to find the optimal location for actuation [39]. The influence of jet location on lift was remarkable at $\alpha = 20°$, with up to 57% increase, but not so noticeable at 18°.

Kamari et al. [40] optimised constant blowing and constant suction on the SD7003 airfoil at $Re = 6 \times 10^4$ by coupling Genetic Algorithms (GA) with Artificial Neural Networks (ANN) previously trained with a set of almost 45 CFD runs. Optimal constant suction was shown more effective. The same numerical methods were applied to the same airfoil, at the same Reynolds number and SJA parameters by Tadjfar and Kamari [41], but at $\alpha = 13°$ and $16°$ and with two alternative injection configurations, namely tangent and normal to the airfoil surface. Aerodynamic efficiency was the objective/target function. Optimal tangent injection at $\alpha = 13°$, produced an astonishing maximum aerodynamic efficiency increase of 591%.

Perhaps the latest, and possibly the most extensive, research in the field of AFC application to airfoils is the one undertaken by Tousi et al. [1]. Five SJA parameters were optimised in a coupled fashion for a SD7003 airfoil at $Re = 6 \times 10^4$ and several pre- and post-stall $\alpha = \{4°, 6°, 8°, 14°\}$ using GA and RANS. The key difference between Tadjfar and Kamari [41] and Tousi et al. [1] resides in the methodology employed. While the former used ANN to estimate most of the SJA AFC parameters, the latter based the entire optimisation process on precise RANS-CFD simulations with the Spalart-Allmaras (SA) turbulence model, which enhances the accuracy of the results at the cost of incurring a high computational burden. This is the first time, to the best of our knowledge, that genetic algorithms have been coupled with an unsteady RANS CFD solver with the aim of optimally tuning a set of SJA AFC parameters to maximise aerodynamic performances of an airfoil in stall conditions. The resulting optimals could not at the time undergo validation against experiments or well-resolved simulations, nor were the flow mechanisms responsible for optimally enhancing aerodynamic performances examined in any detail.

The study presented here builds up on the optimal SJA AFC configurations found by Tousi et al. [1]. Their analysis implicitly relied on the dubious accuracy of RANS-SA simulations of massively detached wake flows and/or deploying SJA AFC. Literature recommendations as to the setup of computations in regards to the tuning of turbulence model parameters and the prescription of free-stream turbulent viscosity boundary conditions were blindly followed. Here we undertake the ensuing natural step and put the optimisation results thus obtained to the test. We analyse optimal SJA on the SD7003 at $Re = 6 \times 10^4$, at a single post-stall $\alpha = 14°$, with accurate, well-resolved, 3D-LES computations. The object is two-fold. On one side, we evaluate the reliability of RANS-SA simulation in assessing SJA application to airfoils in post-stall conditions at moderate Reynolds numbers. On the other hand, we exploit the higher accuracy of LES simulation to better understand the physics behind SJA AFC application to the SD7003 airfoil.

A wealth of numerical and experimental data is available on the literature for the SD7003 airfoil (see, for example, [33,34,42–46]), which makes it a particularly convenient choice for the study of AFC. The SD7003 is a thin airfoil with a thickness-to-chord ratio $t/C = 8.5\%$ that is often employed in micro air vehicles (MAV) intended to fly at moderate Reynolds numbers. A LSB forms on the suction side at low Reynolds number, even for low to moderate values of α. The strong adverse pressure gradient existing beyond the suction peak on the upper surface causes the laminar boundary layer to detach, but separation is shortly followed by turbulent transition and this induces reattachment. The LSB drifts towards the leading edge and shrinks as α increases. Above a critical value of α, however, the reattachment ceases to occur and the recirculation region bursts and extends into the wake, which results in a sharp drop of lift and a dramatic surge of aerodynamic drag.

The remainder of the paper is structured as follows. The governing equations for LES and RANS-SA turbulence models are presented in §2. Section §3 is devoted to the computational domain, boundary conditions and grid assessment. The results and conclusions are presented in §4 and §5, respectively.

2. Governing equations and numerical modelling

The Navier-Stokes equations for an incompressible Newtonian fluid of density ρ and dynamic viscosity μ ($\nu \equiv \mu/\rho$ is the kinematic viscosity) read

$$\nabla \cdot \mathbf{u} = 0, \tag{1}$$

$$\rho \frac{\partial \mathbf{u}}{\partial t} + \rho(\mathbf{u} \cdot \nabla)\mathbf{u} = -\nabla p + \nabla \cdot (\mu \nabla \mathbf{u}). \tag{2}$$

The advection term can be expressed in conservation form by applying the vector calculus identity $(\mathbf{u} \cdot \nabla)\mathbf{u} = \nabla \cdot (\mathbf{u} \otimes \mathbf{u}) - \cancel{(\nabla \cdot \mathbf{u})}\mathbf{u}$, where $\otimes$ denotes the outer product and the divergence term cancels out due to incompressibility. Taking the ensemble average of the Navier-Stokes equation or applying spatial filtering, yields

$$\nabla \cdot \overline{\mathbf{u}} = 0, \tag{3}$$

$$\rho \frac{\partial \overline{\mathbf{u}}}{\partial t} + \rho \nabla \cdot (\overline{\mathbf{u}} \otimes \overline{\mathbf{u}} + \overline{\mathbf{u} \otimes \mathbf{u}}) = -\nabla \bar{p} + \nabla \cdot (\mu \nabla \overline{\mathbf{u}}), \tag{4}$$

where the linear averaging/filtering operator commutes with all operators but the nonlinear term. Switching back to the non-conservation form of the ensemble averaged/filtered advective term following $\nabla \cdot (\overline{\mathbf{u}} \otimes \overline{\mathbf{u}}) = (\overline{\mathbf{u}} \cdot \nabla)\overline{\mathbf{u}} + \cancel{(\nabla \cdot \overline{\mathbf{u}})}\overline{\mathbf{u}}$ and rearranging terms, results in

$$\nabla \cdot \overline{\mathbf{u}} = 0, \tag{5}$$

$$\rho \frac{\partial \overline{\mathbf{u}}}{\partial t} + \rho(\overline{\mathbf{u}} \cdot \nabla)\overline{\mathbf{u}} = -\nabla \bar{p} + \nabla \cdot (\mu \nabla \overline{\mathbf{u}} - \rho \overline{\mathbf{u} \otimes \mathbf{u}}). \tag{6}$$

Here, $-\rho\overline{\mathbf{u} \otimes \mathbf{u}}$ is the Reynolds stress tensor, which must be modelled using a turbulence model for RANS or a subgrid scale (SGS) model in the case of LES. The turbulence models used in the present RANS and LES are the Spalart-Allmaras (SA) [47] and the Wall-Adapting Local Eddy-Viscosity (WALE) [48], respectively. The accuracy of the former was assessed as acceptable in an earlier study [1], but the choice of LES in the present study is based on its demonstrated capabilities in dealing with turbulent transition as well as unstructured grids [48]. The WALE model is based on a tensor invariant that reproduces correctly wall asymptotic behaviour.

Both turbulence models used by either of the CFD methods employed here approximate the Reynolds stress tensor using the Boussinesq hypothesis, which states that the deviatoric part of the tensor can be written as

$$-\overline{\mathbf{u} \otimes \mathbf{u}} - \frac{1}{3}(\nabla \cdot \mathbf{u})\mathbf{I} = -2\nu_t \mathbf{S}. \tag{7}$$

$\mathbf{I}$ denotes the identity matrix, $\mathbf{S} = 1/2\left(\nabla\overline{\mathbf{u}} + \nabla(\overline{\mathbf{u}})^T\right)$ is the rate-of-strain tensor, and ν_t is the turbulent kinematic viscosity scalar field, which is the target of the so-called turbulent viscosity models.

The RANS SA model solves a single transport equation for a modified form of the turbulent kinetic viscosity $\tilde{\nu}$ that is the same with ν_t everywhere but in the near-wall region where viscosity effects dominate. Both turbulent viscosities are related by $\nu_t = \tilde{\nu} f_{v1}$, where $f_{v1} = \chi^3/(\chi^3 + C_{v1}^3)$, $\chi = \tilde{\nu}/\nu$ and $C_{v1} = 7.1$. On the other hand, the LES WALE model, instead of solving a transport equation for ν_t, it models it via SGS, based on the following expression

$$\nu_t = \nu_{sgs} = (C_w \Delta)^2 \frac{\left(\mathcal{S}^d : \mathcal{S}^d\right)^{3/2}}{(\mathbf{S} : \mathbf{S})^{5/2} + \left(\mathcal{S}^d : \mathcal{S}^d\right)^{5/4}} \tag{8}$$

where $\mathcal{S}^d = \frac{1}{2}\left[(\nabla\overline{\mathbf{u}})^2 + (\nabla(\overline{\mathbf{u}})^T)^2\right] - \frac{1}{3}(\nabla \cdot \bar{\mathbf{u}})^2\mathbf{I}$ is the traceless symmetric part of the square of the velocity gradient tensor, $\Delta = \sqrt{\Delta x \Delta y \Delta z}$ is the cut-off width used for filtering the flow field, and Δx, Δy and Δz denote grid sizing along the three orthonormal coordinates. The sole parameter of the model has been set to $C_w = 0.325$, which is a standard choice [49,50]. For the RANS-SA optimisation simulations we initially set the free-stream turbulent viscosity to a very low value $\tilde{\nu}/\nu = 10^{-20}$ following Catalano and Tognaccini [51], who claimed that this was required to properly capture the LSB at low pre-stall α, only to find out at the end that the choice was not the most appropriate for post-stall actuated cases.

Numerical computations have been carried out using the OpenFOAM [52] computational fluid dynamics (CFD) solver, which is based on the finite volume method (FVM). LES has been implemented on an unstructured grid using the Linear-Upwind Stabilised Transport (LUST) [52] scheme in discretising the non-linear advective term. This scheme stabilises the solutions while retaining second-order accuracy. Second-order central-differences has been employed for the diffusive term, and an implicit second-order Backward Euler method has been chosen for evolving the equations in time. The pressure-velocity coupling problem has been tackled by the Pressure-Implicit algorithm with Splitting of Operators (PISO) [53]. The stopping criteria for both the pressure and velocity residuals was 10^{-6}.

For the RANS SA simulations, the same discretisation methods were used as for the preliminar optimisation study by Tousi et al. [1]. These were second order discretisation schemes for

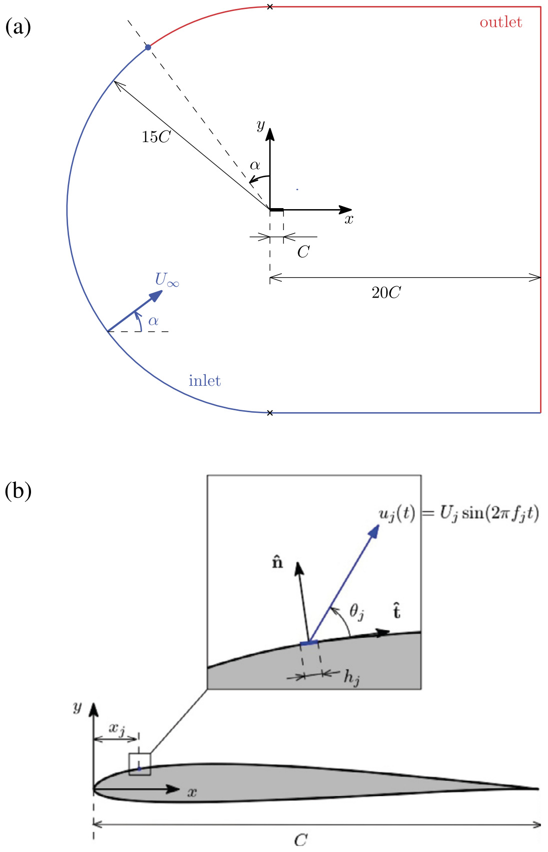

Fig. 1. (a) Computational domain. (b) Synthetic jet parameters. (For interpretation of the colours in the figure(s), the reader is referred to the web version of this article.)

all parameters, and the pressure-velocity coupling PISO scheme, which can cope with transient simulations as required. The averaged solutions presented in the results section, obtained from either LES or SA simulations, are all considered after all initial transients have been overcome.

Each one of the 360 RANS computations required about 84CPUh of supercomputing time at Marenostrum IV – Barcelona Supercomputing Centre, while LES cases consumed 660kCPUh apiece.

3. Domain, boundary conditions and mesh validation

For simplicity, the SD7003 chord length has been taken as $C = 1$ and the free-stream velocity as $U_\infty = 1$ so that the Reynolds number is simply set as $Re = U_\infty C/\nu = 1/\nu = 6 \times 10^4$ and all simulation parameters (including time and space coordinates) and results are already non-dimensional with length and time-scales C and C/U_∞, respectively. The computational domain used for both LES and RANS simulations is depicted in Fig. 1. The airfoil (thick black line) is placed with its chord line horizontal and its leading edge at the coordinate origin $(x, y, z) \equiv (0, 0, 0)$. The two-dimensional spanwise projection of the domain is delimited upstream by a half circle of radius $R = 15$ and centred at the origin, two horizontal lines above and below at $y = \pm 15$ and a vertical line downstream at $x = 20$. The angle of attack is prescribed by tilting the inlet velocity, so that the inlet (blue line) and outlet (red) boundaries are not coincident with the geometrical elements just described (Fig. 1a). For the 3D LES computations, a periodic span of 0.2 has been considered, as this size was shown sufficient for capturing the largest spanwise length scales of the flow at $\alpha = 14°$ and $Re = 6 \times 10^4$ [42,2].

The usual boundary conditions have been applied. At inlet (blue line), a uniform velocity profile of free-stream velocity $U_\infty = 1$ and tilt $\alpha = 14°$ has been prescribed, along with zero normal pressure gradient ($\nabla p \cdot \hat{\mathbf{n}} = 0$). At outlet, the roles of pressure and velocity are reversed, so that homogeneous Dirichlet boundary condition is used for pressure ($p = 0$) and homogeneous Neumann ($\nabla \mathbf{u} \cdot \hat{\mathbf{n}} = \mathbf{0}$) for velocity. The airfoil surface is treated as an impermeable no-slip wall by setting both velocity ($\mathbf{u} = 0$) and the normal gradient of pressure to zero. On the upper surface of the airfoil, a short portion of length the jet slot width h is cut straight and switched to inlet-type boundary conditions at the jet location for the actuated cases. Here, the time-dependent jet velocity $u_j = U_j \sin(2\pi f_j t)$ is prescribed, with $2U_j$ the jet velocity amplitude and f_j the actuation frequency. The jet velocity is tilted at an angle θ_j with respect to the airfoil surface and the velocity profile simply taken as a top-hat function in the streamwise direction and uniform along the wing span. Homogeneous Neumann boundary conditions are used for pressure at the jet boundary. Finally, periodic boundary conditions are enforced to the lateral boundaries of the domain for three-dimensional simulations.

A sketch representing the synthetic jet design parameters is presented in Fig. 1b. These parameters are the jet location along the chord x_j, the jet width h_j, and the jet angle θ_j (with respect to the airfoil surface), frequency f_j, and momentum coefficient $C_\mu = (h_j \rho_j U_j^2 \sin\theta_j)/(C\rho U_\infty^2)$, with the jet fluid density $\rho_j = \rho = 1$ the same as free-stream density on account of incompressibility.

An unstructured computational grid, consisting of about 28.7 million control volumes has been employed for the LES unactuated baseline case. The mesh was highly refined around the airfoil and along the wake, but left to coarsen in the far-field, as shown in Fig. 2. For the actuated cases, cell count has been increased to nearly 30 million due to the higher grid resolution required to resolve the jet. The spanwise length has been discretised into 48 layers, as shown adequate by previous simulations for this same airfoil at the same Reynolds number and angle of attack [42].

According to Piomelli and Chasnov [54], the near-wall mesh resolution required for wall-resolved LES simulations involving mainly attached boundary layers is $\Delta x^+ = \mathcal{O}(50 - 150)$, $\Delta y^+ < 2$, and $\Delta z^+ = \mathcal{O}(15 - 40)$, where the $+$ superscript denotes wall units. The first cell layer thickness in wall units is $\Delta y^+ = y u_\tau/\nu$, where y is the dimensional normal distance to the wall, $u_\tau = \sqrt{\tau_w/\rho}$ is the friction velocity and τ_w the wall shear stress. Δx^+ and Δz^+ characterise the wall-grid spacing in the streamwise and spanwise directions, respectively, and are obtained from dimensional grid spacing in the same way as Δy^+. The maximum Δx^+, Δy^+ and Δz^+ on the upper surface of the airfoil are about 0.2, 0.5 and 18, respectively. The excess resolution in the streamwise wall-parallel direction could have been avoided by resolving the near-wall region with a structured mesh of prisms, which would have resulted in a lower cell count, but due to the massively separated nature of the baseline flow we deemed it prudent to keep cells short.

The resolved-to-total turbulent kinetic energy (TKE) ratio ($k_{\text{res}}/k_{\text{tot}}$ where $k_{\text{tot}} = k_{\text{res}} + k_{\text{sgs}}$, the total kinetic energy, is the sum of the resolved and modelled parts) provides yet another means of assessing LES mesh quality. The resolved component of TKE is obtained from the velocity field fluctuations of the resolved scales as $k_{res} = \left(\langle u'u' \rangle + \langle v'v' \rangle + \langle w'w' \rangle\right)/2$, whereas the modelled component is $k_{\text{sgs}} = \nu_{\text{sgs}}/C_k\Delta$. The model parameter was set to a standard $C_k = 0.094$, which combined with the also standard value for $C_\epsilon = 1.048$ results in the classic value for the Smagorinsky constant $C_s = C_k^3/C_\epsilon = 0.1677$. Sound LES simulations should resolve at least 80% of TKE [55], and this is the case of our baseline simulation, as clearly shown in Fig. 3. The mesh was sufficiently fine to resolve above 95% of TKE in all cases, leaving less than 5% to the sub-grid scale model in the most critical regions, namely the proximal part of the shear layer after boundary layer separation.

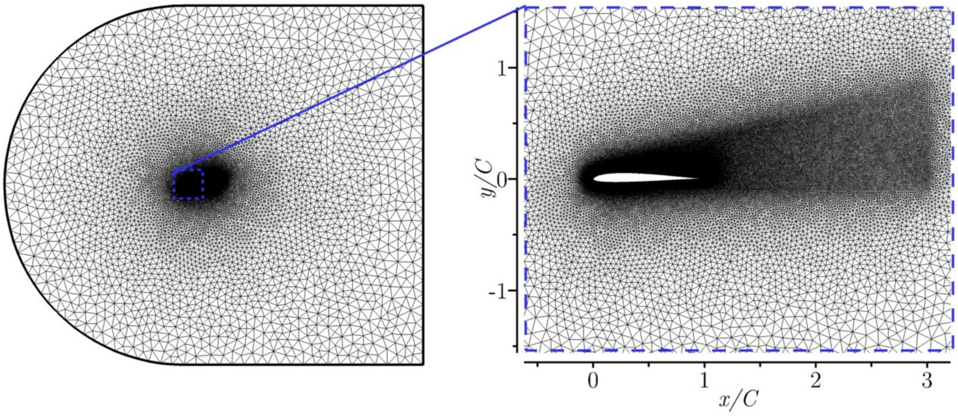

Fig. 2. An overview of LES baseline mesh along with a zoomed view of its near-wall and wake regions.

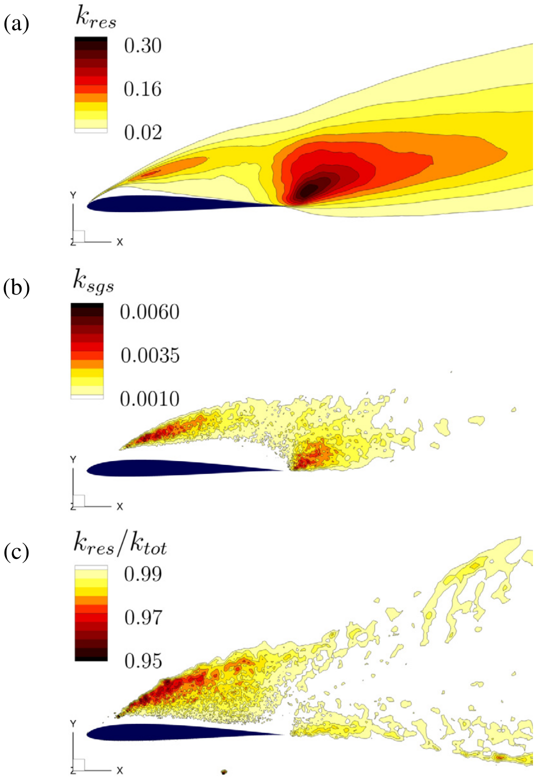

Fig. 3. Resolved k_{res} and b) modelled k_{sgs} parts of the turbulent kinetic energy (TKE). c) Resolved-to-total TKE ratio $k_{\text{sgs}}/k_{\text{tot}}$.

The Courant-Friedrichs-Levy number was limited to CFL<0.8 by means of an adaptive time-stepper.

The mesh-independence and time-resolution analyses for the 2D RANS-SA simulations were performed and reported in an earlier study [1], concluding that a hybrid mesh of 45,466 cells and a time step $\Delta t = 2 \times 10^{-5}$ was sufficient to properly capture the flow dynamics and to resolve boundary layers down to the viscous sublayer. The mesh truncation error was estimated at about 0.01% (see table 1 of that paper).

The baseline LES case has been validated against the simulations by Rodriguez et al. [2] and Galbraith and Visbal [42], both corresponding to the same airfoil at the same Reynolds number and angle of attack. The former study employed LES on a grid of nearly 30 million nodes, while the latter used Implicit LES (ILES) on a more modest mesh of about 5.7 million grid points. The values of time-averaged lift (C_l) and drag (C_d) coefficients, along with aerodynamic efficiency ($\eta = C_l/C_d$) and the Strouhal number or von Kármán frequency of vortex shedding (f_{vK}), are presented in Table 1. Current baseline simulation shows very good agreement with Rodriguez et al. [2] (within 1%) and a fairly good match with ILES simulations by Galbraith and Visbal [42]. The mesh and numerical approaches undertaken are sufficiently different that the mesh truncation error can be trusted to be contained within reported discrepancies for average aerodynamic performance parameters and, therefore, amount to less than 1%. RANS-SA results, however, tend to underestimate both aerodynamic force coefficients, particularly so C_d.

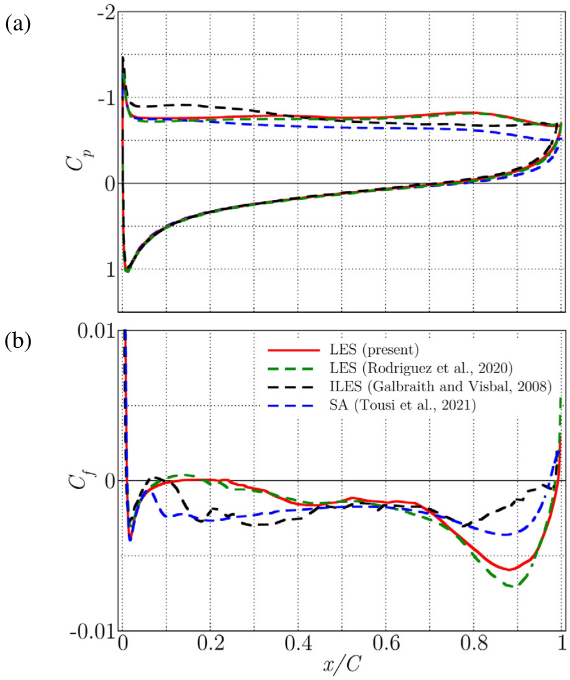

Fig. 4. Spanwise- and time-averaged chord distributions of (a) pressure C_p and (b) skin friction C_f coefficients along the SD7003 surface(s) at $Re = 6 \times 10^4$ and $\alpha = 14°$. Shown are the present LES (solid red), the LES case by Rodriguez et al. [2] (dashed green), ILES by Galbraith and Visbal [42] (dashed black) and SA RANS by Tousi et al. [1] (dashed blue).

Aggregate quantities such as forces are always prone to misleading conclusions due to unnoticed compensation. Local quantities convey a better degree of appreciation as to whether the flow dynamics are being adequately captured. Fig. 4a depicts the chord distribution of the spanwise averaged pressure coefficient $C_p = (p - p_\infty)/(0.5\rho U_\infty^2)$ along both upper and lower surfaces. No apparent differences exist among the various simulations considered for the C_p distribution on the lower surface, except perhaps

Table 1
Literature review of the aerodynamic performances of the SD7003 airfoil at $Re = 6 \times 10^4$ and $\alpha = 14°$. L_x, L_y and L_z are the domain size in the streamwise, cross-stream and spanwise directions, respectively, in units of C. N_{xy} and N_z are the in-plane and spanwise resolutions, and T the time-span of the simulations in C/U_∞ units.

	Domain	$L_x \times L_y$	L_z	N_{xy}	N_z	T	C_l	C_d	f_{vK}	η
LES FVM (Present)	C-grid	35×30	0.2	597,916	48	35	0.895	0.239	0.69	3.744
LES FEM [2]	H-grid	15×16	0.2	467,812	64	65	0.886	0.238		3.726
ILES FDM [42]	O-grid	30×30	0.2	47,565	101	15	0.875	0.221		3.960
2D-RANS-SA [1]	C-grid	35×30	-	45,466	-	60	0.798	0.204		3.911

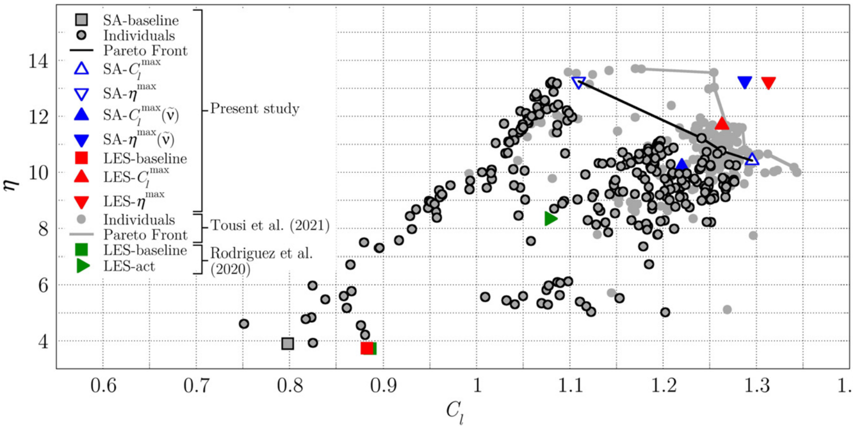

Fig. 5. Optimisation procedure and optimal cases in objective function space (C_l, η).

very slightly in the vicinity of the trailing edge. On the upper surface, the match between present results and Rodriguez et al. [2] is remarkably accomplished, while the ILES of Galbraith and Visbal [42] and the 2D RANS-SA by Tousi et al. [1] are fair but not excellent due to the less precise computational methods employed and the coarser grids. The aforementioned compensation effect is clear for the simulation by Galbraith and Visbal [42], which clearly transfers some lift from the back of the airfoil to the front. The resulting C_l is about the same obtained in the LES simulations, but at the cost of a nose-up shift of the pitching moment coefficient C_m. The skin friction coefficient $C_f = \tau_w/0.5\rho U_\infty^2$ again shows a fair agreement with Rodriguez et al. [2]. The boundary layer separation on the upper surface is, on average, located at $x_{\text{sep}} \simeq 0.011$, and is also fairly well predicted by ILES and RANS-SA simulations, although downstream from the separation point these present noticeable discrepancies with respect to the two LES simulations. This may challenge the alleged capabilities of RANS-SA to properly reproduce highly separated flows, at least from a quantitative point of view, but since actuation is intended to reduce or even suppress separation, the method might still work acceptably for actuated cases.

4. Results

An optimisation procedure was employed by Tousi et al. [1] to determine optimal SJA parameters in terms of maximising both C_l and η. The set of five SJA parameters, the design variables of the optimisation problem, comprises the actuation frequency f_j, the jet inclination angle with respect to the airfoil surface θ_j, the slot streamwise location measured from the airfoil leading edge x_j, the jet slot width h_j and the jet momentum coefficient $C_\mu \equiv (\rho_j U_j^2 h_j \sin\theta_j)/(\rho_\infty U_\infty^2 C)$. The method coupled a scripted mesh generator (GMSH [56]), a CFD package (OpenFOAM) and a Genetic Algorithm (GA). The GA population size was set to 20 individuals (each one consisting in a CFD case with a different set of prescribed SJA parameters) per generation/iteration, which was considered a reasonable trade-off between method performance and computational cost. The first generation was initialised with a random set of individuals, and all CFD cases run. The two objective functions, C_l and η, were obtained for each of the simulations and passed onto the GA optimiser, where the *Selection*, *Crossover* and *Mutation* operators were applied to produce a new set of values for the five SJA parameters defining the individuals for the next generation. The Selection phase employed a $\mu + \lambda$ strategy with a *Crowded-Comparison* Operator [57]. Simulated Binary Crossover (SBX) [58] (with a probability of 0.9) and Polynomial Mutation [59] (with a probability of 0.1) were adopted for the Crossover and Mutation phases, respectively. This process was repeated until having completed 18 generations (360 CFD simulations), the overall improvement being found marginal after the sixteenth generation. For a detailed account of the optimisation method used, we refer the reader to Tousi et al. [1]. Each additional individual requires a full CFD simulation, such that aspiring to be overly accurate results in unfeasible optimisation time spans. For this reason, a compromise was done by using two-dimensional RANS simulations with the Spalart-Allmaras model.

Fig. 5 presents a summary of the results obtained along the optimisation process, as seen in objective function space. The 2D RANS-SA baseline case (grey-filled black square) starts at low values of both C_l and η. Actuated cases (grey-filled black circles corresponding to the 360 cases run) progressively move to higher lift coefficient and aerodynamic efficiency values to finally delineate a multi-objective Pareto front (black line) with optimum C_l (up-pointing empty blue triangle) and maximum η (down-pointing empty blue triangle). The optimisation was run further by Tousi et al. [1] by increasing the initial set of 360 cases with an additional 240 runs thus reaching a final population of up to 600 individuals (grey circles and grey line for the second Pareto front), but the final results were still not available by the time the present study began, and the further refinement obtained was anyway expected to be within the accuracy limits of RANS-SA. The LES baseline case (red square), as for Rodriguez et al. [2] (green square), has a larger C_l than the 2D RANS-SA case, as already pointed out, so that it is to be expected that some discrepancies might be encountered when switching from RANS-SA to LES for the optimally actuated cases. In any case, the LES non-optimised actuated case

Table 2
Baseline case, and optimal SJA actuation cases corresponding to maximum lift $C_l^{\max}$ and maximum aerodynamic efficiency $\eta^{\max}$. The values of the five actuation parameters (jet frequency f_j, jet momentum coefficient C_μ, jet inclination angle with respect to the airfoil surface θ_j, jet streamwise location from leading edge x_j and jet slot width h_j) are listed alongside the resulting aerodynamic performances.

	SJA parameters					Aerodynamic performance parameters				
	f_j	C_μ	θ_j (°)	x_j	h_j	C_l	C_d	η	$\Delta C_l/C_l$	$\Delta\eta/\eta$
Baseline										
SA [1]						0.798	0.204	3.91		
LES (present)						0.895	0.239	3.74		
LES [2]						0.886	0.238	3.72		
Actuated										
SA-$C_l^{\max}$	1.6	0.0053	53	0.0097	0.005	1.295	0.129	10.42	+62.3%	+157.4%
SA-$C_l^{\max}(\tilde{\nu})$						1.220	0.1194	10.21	+52.9%	+161.1%
LES-$C_l^{\max}$						1.263	0.108	11.69	+41.1%	+212.5%
SA-$\eta^{\max}$	2.6	0.0055	18	0.0089	0.005	1.109	0.083	13.25	+31.1%	+239.7%
SA-$\eta^{\max}(\tilde{\nu})$						1.288	0.097	13.27	+61.4%	+239.4%
LES-$\eta^{\max}$						1.313	0.094	13.96	+46.7%	+273.2%
LES-[2]	1.0	0.0030	90	0.0070	0.007	1.078	0.129	08.35	+21.6%	+124.4%

run by Rodriguez et al. [2] (green triangle) falls largely short of the results expected from the optimisation.

The optimum SJA parameters at either end of the Pareto Front, corresponding to cases SA-$C_l^{\max}$ and SA-$\eta^{\max}$, and the resulting aerodynamic performances are presented in Table 2. The case featuring maximum lift achieved a considerable improvement $\Delta C_l/C_l = 62.3\%$ with respect to baseline. Beside improving lift, this actuation setup also enhances aerodynamic efficiency by $\Delta\eta/\eta = 157.4\%$. Meanwhile, the maximum aerodynamic efficiency case boosted it by an impressive $\Delta\eta/\eta = 239.7\%$, retaining still an appreciable $\Delta C_l/C_l = 31.1\%$ increase in lift. Three of the SJA parameters, namely $C_\mu \simeq 0.005$, $x_j \simeq 0.009$ (just upstream of the separation point) and $h_j \simeq 0.005$, take essentially the same value for the two optimal cases considered. The main differences concern the actuation frequency f_j and injection angle θ_j. Maximum efficiency is obtained by actuating almost tangentially with $\theta_j = 18°$ at frequency $f_j = 2.6$, while maximum lift requires larger actuation angle $\theta_j = 53°$ and lower frequency $f_j = 1.6$.

Since the optimally actuated RANS-SA cases might be afflicted by the same shortcomings that plague the baseline run, two LES simulations at the same optimal set of actuation parameters were also undertaken. The results are indicated in Fig. 5 (up-pointing and down-pointing red triangles for the $C_l^{\max}$ and $\eta^{\max}$ cases, respectively) and accordingly listed in Table 2. While both LES simulations outperformed amply the unoptimised actuated case by Rodriguez et al. [2], the results notably differ from the 2D RANS-SA estimation. While the maximum lift case produced slightly lower C_l and somewhat higher η, the maximum aerodynamic efficiency case yielded remarkably higher C_l without notably modifying η. As a result, the latter case became at once optimal in terms of both C_l and η.

It must be born in mind that optimisation techniques for non-linear problems, GA being no exception, provide no guarantee that the best SJA configuration found is indeed optimal, let alone the absolute optimum. The configurations selected here as *optimal* are thus tagged in the weaker sense that nearly doubling the GA population of RANS-SA individuals did not produce better aerodynamic performances [1] than those obtained here for the two LES cases tested and, more importantly, that the well-resolved simulations widely outperformed available sub-optimal results for the same airfoil and flight conditions.

The discrepancies between 2D RANS-SA and LES simulations, also for the actuated cases, dispute the applicability of the former to low Reynolds number aerodynamics past airfoils at post-stall conditions, even in situations for which boundary layers remain attached through the action of SJA. RANS is specifically designed for turbulent flow conditions, and performs reasonably provided the model parameters are appropriately tuned. Some models can deal with laminar-turbulent transition, but their reliability is largely dependent on parameter tuning. In the case of the SA turbulence model, this sensitivity extends crucially to the free-stream boundary conditions for the unique turbulent field $\tilde{\nu}$. Following Catalano and Tognaccini [45,51], which states that free-stream turbulent viscosity must be sufficiently low so as to properly capture the LSB at pre-stall α, we set $\tilde{\nu}/\nu = 10^{-20}$ for the SJA optimisation RANS simulations. As it happens, the optimisation process was run in post-stall conditions and with a time-dependent fluidic actuation that crucially acts on the LSB. Such a low turbulent viscosity might be artificially stabilising the laminar flow region and thus inducing wrong results. To check sensitivity to free-stream preturbulence levels, the baseline, maximum lift and maximum aerodynamic efficiency cases were run for a wide range $\tilde{\nu}/\nu \in [10^{-20}, 10^2]$. The results are presented in Fig. 6. Unrealistically high free-stream turbulent viscosity of the order of the fluid viscosity and above ($\tilde{\nu}/\nu \geq 1$) produces unphysical results and must be discarded. At the low-values end of the range, RANS-SA results (blue lines) are fairly stable but diverge considerably from LES (red horizontal lines). Not much is gained at intermediate levels of $\tilde{\nu}/\nu$ for the baseline case, which produces pretty stable but wrong C_l and C_d values all along. The actuated cases, however, traverse a regime $\tilde{\nu}/\nu \in [10^{-6}, 10^{-3}]$ with RANS-SA C_l and C_d values decently close to LES results. The aerodynamic performance of the maximum lift and maximum aerodynamic efficiency cases for $\tilde{\nu}/\nu = 10^{-5}$ are shown in Fig. 5 (filled blue symbols) and listed in Table 2 as SA-$C_l^{\max}(\tilde{\nu})$ and SA-$\eta^{\max}(\tilde{\nu})$, respectively. If not quite on top of the LES results, they at least are much closer and clearly align with the trend. The deviation from the original RANS-SA optimals as obtained from a reduced population of 360 individuals serves as an *a-posteriori* justification for not having waited for the completion of the 600 runs before starting the two *optimal* LES cases. It is clear enough that the error incurred by using RANS-SA in the optimisation process is sufficiently large and unsystematic to consider both Pareto fronts, the preliminar and the refined, as not significantly distinct. The reason for this better agreement between RANS-SA and LES at intermediate values of the free-stream turbulent viscosity, only for actuated cases, remains a mystery. Unfortunately, the apparent improvement of the RANS-SA model with a more appropriate choice for $\tilde{\nu}$ was not known at the time the optimisation process was run and it was later thought inexpedient, on cost-benefit grounds, to re-run it anew. Besides, there is no guarantee that this same value of $\tilde{\nu}/\nu$ will produce accurate results at other post-stall flight regimes or under different SJA operat-

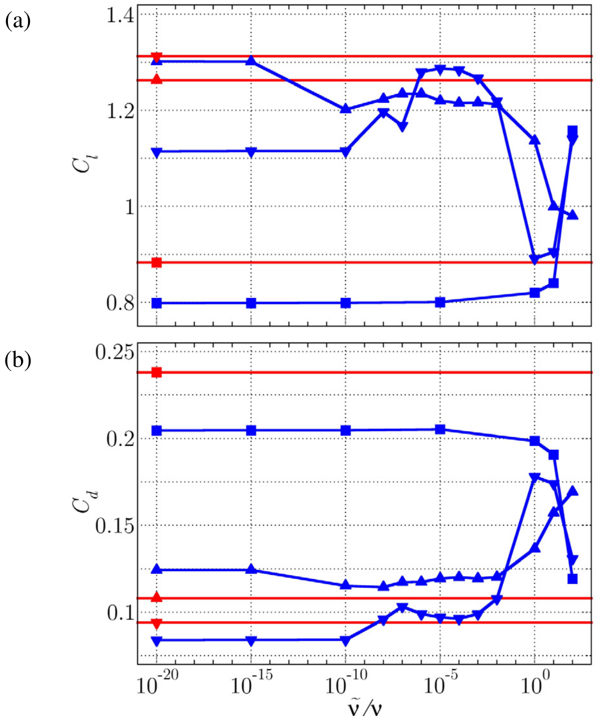

Fig. 6. Results sensitivity to free-stream preturbulence levels as prescribed by $\tilde{\nu}/\nu$. (a) Average lift coefficient C_l. (b) Average drag coefficient C_d. Baseline (squares), maximum lift (up-pointing triangles) and maximum aerodynamic efficiency (down-pointing triangles) SJA setups are shown for both RANS-SA (blue) and LES (red) computations.

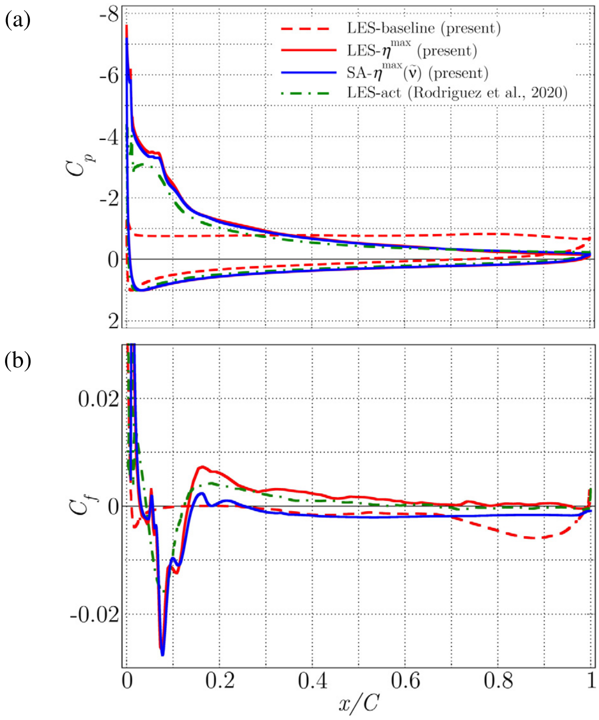

Fig. 7. Optimal SJA vs baseline (a) Pressure C_p and (b) skin friction C_f coefficient distributions. Shown are the LES-baseline (dashed red), the LES-$\eta^{\max}$ (solid red), RANS SA-$\eta^{\max}(\tilde{\nu})$ (solid blue) and sub-optimal actuated LES-act case by Rodriguez et al. [2] (dash-dotted green).

ing conditions. A thorough parametric exploration, far beyond the scope of this study, will be required to cast light on the issue. Breuer [35] observed that high inlet turbulent intensities tend to reduce and even suppress the LSB on the upper surface of the unactuated airfoil. This would explain the sharp drop of C_d and the surge of C_l we observe for the baseline case when high values of $\tilde{\nu}$ are prescribed at inlet. The LSB shrinks and vanishes and the airfoil performs as in pre-stall conditions on account of the turbulent boundary layer and the delay in its separation. For actuated cases, too high free-stream $\tilde{\nu}$ over-rides the SJA capabilities and the airfoil behaves much as in the baseline case, all the more so for maximum efficiency SJA.

In the remaining of the manuscript, RANS-SA optimal cases have been considered for $\tilde{\nu}/\nu = 10^{-5}$ instead of the original runs used for optimisation. Furthermore, since the maximum aerodynamic efficiency case outperforms the maximum lift case in all respects when assessed with these new RANS-SA or LES simulations, only the corresponding set of SJA parameter values will be considered further, as an absolute optimum.

4.1. RANS-SA vs LES comparison of optimally actuated cases

The pressure and skin friction coefficient distributions along the upper and lower surfaces corresponding to the maximum efficiency SJA set of parameters are plotted in Fig. 7 alongside baseline LES results (dashed red line). As expected, SJA manages to reattach the flow over a large portion of the upper surface. The separation point, identified by $C_f = 0$, is retarded for all three actuated simulations, LES-$\eta^{\max}$ (solid red), SA-$\eta^{\max}(\tilde{\nu})$ (solid blue) and the sub-optimal LES-act case by Rodriguez et al. [2] (dash-dotted green), with respect to baseline (dashed red line). The separation bubble, though, is short and reattachment is effected shortly behind the jet location. The reattachment contributes to slightly increasing the pressure on the lower surface and, more notably, to enhancing the suction effect on the upper surface, particularly so along the front half of the airfoil. Suction on the back half is reduced but the net effect is that of a lift increase and a sharp pressure drag reduction. All three SJA cases show similar features. In particular, the SA-$\eta^{\max}(\tilde{\nu})$ and LES-$\eta^{\max}$ computations, run with the same SJA parameter values, present very similar pressure distributions, which indicates that the main flow features are being appropriately dealt with also by the less accurate RANS-SA model when free-stream turbulent viscosity is appropriately prescribed to a moderate realistic value. The sub-optimal LES-act produces less suction in the front part of the upper surface and therefore lower lift, as a result of its being suboptimal. Friction distributions are very similar for the LES-$\eta^{\max}$ and LES-act cases except around the actuation location, where the different actuation parameters produce very different local outcomes. The SA-$\eta^{\max}(\tilde{\nu})$ reproduces quite accurately the behaviour of C_f in the front part of the airfoil, as comparison with the LES-$\eta^{\max}$ simulation avows, but the reattachment is not properly fulfilled and the friction remains negative over most of the upper surface when it should in reality be small but positive and decisively contribute to friction drag. The effect on total net drag is however not noticeable, as form drag largely dominates. All in all, 2D RANS-SA simulation seems an appropriate cost-effective tool for extensive optimisation of SJA parameters provided an adequate amount of turbulent viscosity is allowed at the inlet of the domain, and final optimal results are further refined with LES (or DNS if feasible).

Fig. 8 shows colourmaps of the $\langle u'v' \rangle$ component of the Reynolds stress tensor along with a collection of time- and spanwise-averaged streamlines for the baseline and maximum aerodynamic efficiency actuated cases. The baseline separation bubble exhibits similar topologies for the LES-baseline and RANS-SA-baseline simulations. The dynamical behaviour, as represented by $\langle u'v' \rangle$, is however quite different. Streamwise-cross-stream cross-correlation is evenly distributed along the shear layer bounding the separation bubble at the top for RANS-SA-baseline, while

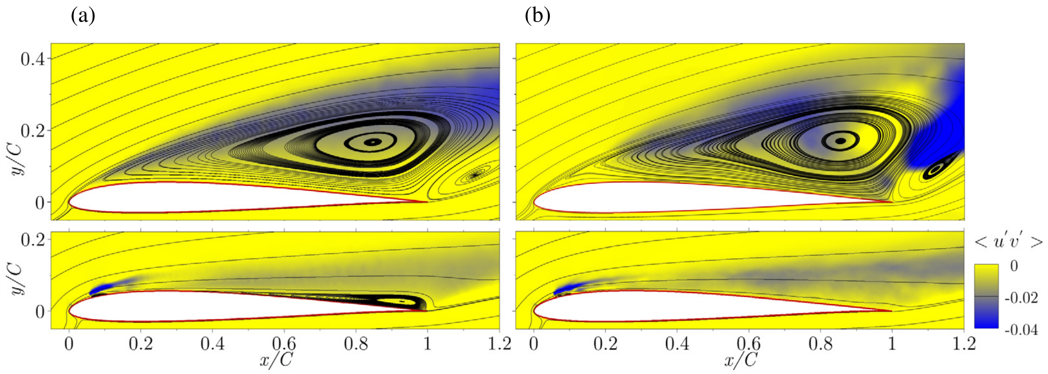

Fig. 8. Spanwise-averaged $\langle u'v' \rangle$ component of the Reynolds stress tensor and time- and spanwise-averaged streamlines. (a) RANS-SA-baseline (top) and RANS-SA-$\eta^{\max}(\tilde{\nu})$ (bottom). (b) LES-baseline (top) and LES-$\eta^{\max}$ (bottom).

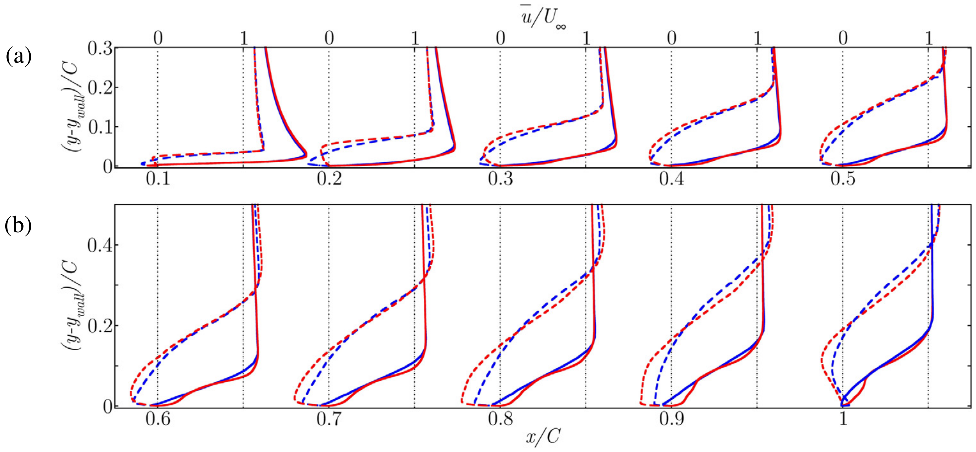

Fig. 9. Evolution of the upper-surface boundary layer along the airfoil. Time- and spanwise-averaged streamwise velocity profiles $\langle u(x, y, z; t) \rangle_{t,z}$ at streamwise coordinates (a) $x/C = 0.1$ through $x/C = 0.5$ and (b) $x/C = 0.6$ through $x/C = 1$, as a function of wall-normal distance. Shown are the baseline (dashed) and actuated (solid) cases, for both LES (red) and RANS-SA (blue) simulations. The actuated cases are LES-$\eta^{\max}$ and SA-$\eta^{\max}(\tilde{\nu})$.

it is much more concentrated in the vortex formation region at the back of the airfoil for LES-baseline. The RANS-SA model is not expected to behave particularly well in post-stall conditions. Once actuation is switched on, the quality of RANS-SA results improves remarkably. The RANS-SA-$\eta^{\max}(\tilde{\nu})$ and LES-$\eta^{\max}$ cases display a very similar distribution of $\langle u'v' \rangle$. These are particularly high in the region of the jet as it bends downstream, blown by the incoming flow. Also streamlines reveal a fairly comparable pattern, except that RANS-SA does not manage to completely suppress the separation bubble and a narrow but relatively long recirculation region extends on the upper surface from the trailing edge upstream. The boundary layer is therefore attached for LES but not for RANS-SA. However, the effects on the pressure distribution are not large, and although the friction on the aft portion of the upper surface differs notably, the net lift and drag, which are pressure dominated, do not suffer exceedingly from the inaccuracies incurred by the RANS-SA model.

To clarify the evolution of the boundary layer along the upper surface of the airfoil, the time- and span-averaged velocity profiles are presented in Fig. 9 at several streamwise locations. The baseline case (dashed lines) has the boundary layer already separated at $x = 0.1$, as clear from the reverse flow in the close proximity of the wall. The LES simulation (red), however, features lower recirculation velocity than the RANS-SA computation (blue), but spread over a wider cross-section. The peak of reverse flow is indeed located further from the wall for LES. These differences between the two methods region remain as the separated cross-section widens downstream all the way down to $x = 0.5$, beyond which point RANS-SA starts underpredicting negative streamwise velocity with respect to LES. Maximum aerodynamic efficiency actuation (solid lines) suppresses separation, notably at $x = 0.2$ and beyond. The reattached boundary layer is very similar for LES and RANS-SA, an indication that the latter method is properly capturing the effects of SJA. The match is very good for $x \leq 0.2$ and gradually deteriorates downstream. Nonetheless, agreement remains acceptable in all respects except for the slight flow reversal RANS-SA predicts in the immediate proximity of the wall over most of the upper surface.

To better characterise the boundary layer in terms of the viscous blockage, the displacement (δ_1) and momentum (δ_2) thicknesses help quantify the near-wall mass-flow and momentum deficits resulting from the effects of viscosity. These are computed following

$$\delta_1 = \int_0^{\delta} \left(1 - \frac{\hat{u}}{\hat{u}_e}\right) d\hat{y}, \tag{9}$$

$$\delta_2 = \int_0^{\delta} \frac{\hat{u}}{\hat{u}_e} \left(1 - \frac{\hat{u}}{\hat{u}_e}\right) d\hat{y}, \tag{10}$$

where $\hat{y}$ is the local wall-normal coordinate, $\hat{u}$ the streamwise (wall-parallel) velocity component, $\hat{u}_e$ its value at the boundary layer edge, and δ the boundary layer thickness, formally infinite but in practice the wall-normal distance required to reach the virtually inviscid flow region. As boundary layer thickness we have used $\delta = \delta_\tau$, defined as the wall-normal distance where the shear

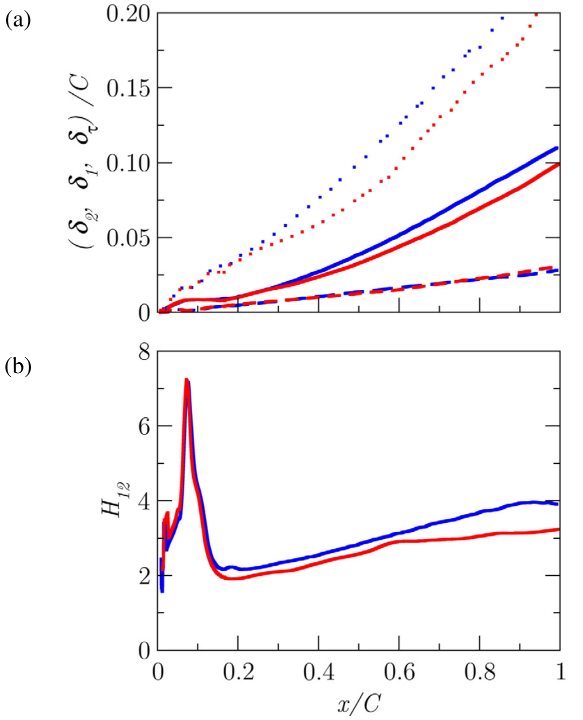

Fig. 10. Evolution of boundary layer characteristic properties along the upper surface of the airfoil for actuated cases LES-$\eta^{\max}$ (red lines) and RANS-SA-$\eta^{\max}(\tilde{\nu})$ (blue). (a) Boundary layer (δ_τ, dotted), displacement (δ_1, solid), and momentum (δ_2 dashed) thicknesses. (b) Shape factor H.

$\|\tau\|$ is seen to decay a 95% with respect to the maximum value recorded on the airfoil surface $\tau_w^{\max}$ ($\|\tau\| < 0.05\tau_w^{\max}$). The evolution of δ_τ, δ_1, δ_2 and the shape factor $H \equiv \delta_1/\delta_2$ along the upper surface is shown in Fig. 10 for both the LES-$\eta^{\max}$ and RANS-SA-$\eta^{\max}(\tilde{\nu})$ cases. All three thicknesses grow steadily along the chord but are much reduced in relation to baseline (not shown in the figure) following the suppression of boundary layer separation. RANS-SA slightly overestimates δ_1 over the aft half of the airfoil and underestimates δ_2 on the last third. As a result, shape factor is larger in this region for the RANS-SA simulation than for LES. The separation bubble visible in Fig. 8 must be held responsible for the discrepancies. It is also interesting to observe that both actuated cases show particularly large Reynolds stresses values at the injection/suction zone, Reynolds stresses are also observed along the airfoil upper surface especially in the LES-*max*η case. This fact explains why the boundary layer remains reattached under these conditions.

4.2. Baseline vs optimally actuated case comparison

The three LES simulations for baseline, (allegedly) maximum lift and maximum aerodynamic efficiency cases have been minutely analysed to elucidate the flow mechanism whereby SJA attains enhanced aerodynamic performances at post-stall angles of attack. In order to characterise the time dependence of the flow, five probe arrays were deployed in the flow field as indicated in Fig. 11a. All five probe lines are located in regions where high fluctuation levels are expected, as indicated by the high values of $\langle u'v'\rangle$. Three are distributed along the shear layer resulting from the early separation of the boundary layer, and the remaining two in the very near wake region. The streamwise ($u_{(x,y)}(z,t)$) velocity signal along spanwise probe arrays P$_2$ (within the shear layer at (x,y)=(0.098,0.08), grey lines) and P$_5$ (in the near wake at $(x, y) = (1.1, 0.08)$, black) have been Fourier-transformed to obtain the Power Spectral Density (PSD) $|\hat{u}_{(x,y)}(z, f)|$ and then spanwise

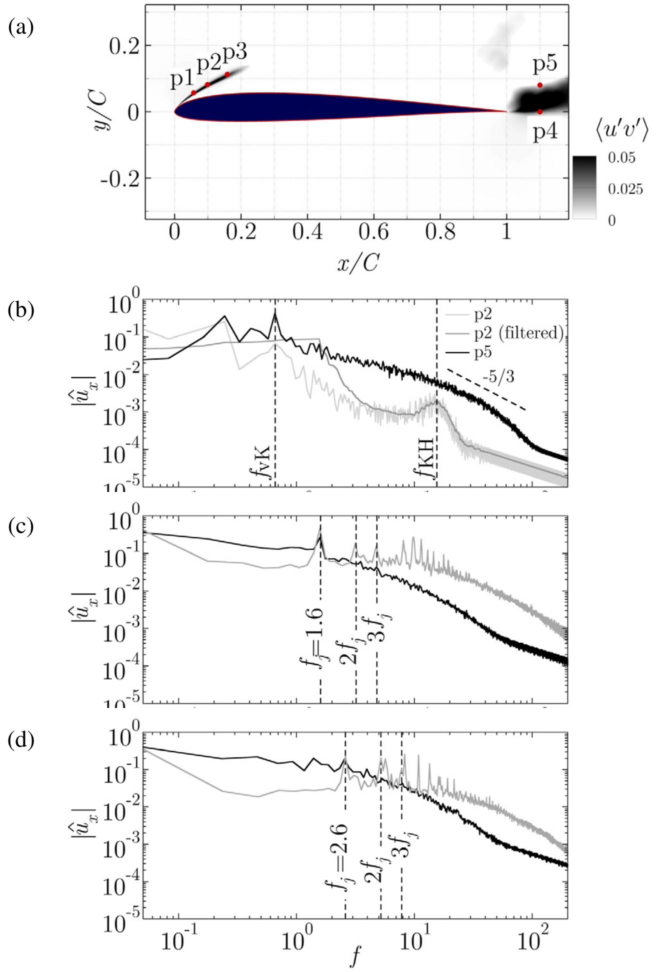

Fig. 11. Power Spectral Density (PSD) of the streamwise velocity signal as recorded from spanwise probe arrays P$_2$ and P$_5$. (a) LES-baseline spanwise-averaged $\langle u'v'\rangle$ colourmap showing the location of the five probe-arrays. Three probes are placed along the shear layer, while the other two are in the very near wake. The PSD of the signals from probes P$_2$ $(x, y) = (0.098, 0.08)$ and P$_5$ $(x, y) = (1.1, 0.08)$ are represented for the (b) LES-baseline, (c) LES-$C_l^{\max}$ and (d) LES-$\eta^{\max}$ cases. Shown are the spectra for the signal read from P$_5$ (black) and P$_2$ (light grey), which has been further filtered (dark grey).

averaged into panels Fig. 11b-d for the LES-baseline, LES-$C_l^{\max}$ and LES-$\eta^{\max}$ cases, respectively. Quadratic interpolation pinpoints the main frequency peaks in the spectrum. For the baseline case, the Strouhal frequency associated with the vortex-shedding of Kármán vortices is identifiable at $f_{\mathrm{vK}} = 0.69$, both at locations P$_2$ and P$_5$. The -5/3 energy slope that is typical of the inertial range of developed turbulence is also noticeable despite the transitional nature of the flow considered here. Probe P$_2$ also detects a broadband peak at about $f_{\mathrm{KH}} = 15.5$ that may be associated with the passage of Kelvin-Helmholtz vortices. In order to precisely detect the f_{KH}, the filtered signal form probe P$_2$ is represented as a dark-grey line in Fig. 11b. Probes P$_1$ and P$_3$ also record the same phenomenon, albeit with decreasing intensity, while P$_4$ and P$_5$ do not in the least reflect it. This is clearly suggestive of a local instability that develops precisely along the shear layer, i.e. a Kelvin-Helmholtz instability.

Actuating with $f_j = 2.6$, as corresponds to the LES-$\eta^{\max}$ case, the jet frequency is imprinted on the flow and recorded at all probes. The vortex-shedding frequency is superseded by actuation, and no wake vortices are discernible. Several harmonics of the jet actuation frequency are also visible in the spectrum of signals recorded close to the actuation location. The same happens for the

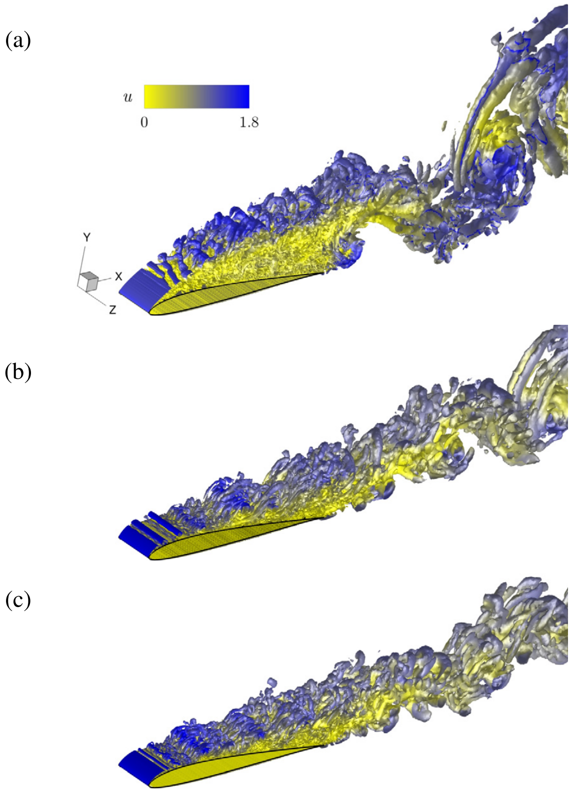

Fig. 12. Instantaneous vortical structures visualised through iso-surfaces of the Q-criterion $Q = 30U_\infty^2/C^2$, coloured by streamwise velocity u. (a) LES-baseline. (b) LES-$C_l^{\max}$. (c) LES-$\eta^{\max}$. (See online movies.)

LES-$C_l^{\max}$, albeit with the reduced frequency $f_j = 1.6$. Again, the main peak is detected at all probes, while harmonics -a large number of them- are only detected by probes that are sufficiently close to the jet location. The actuation frequency for maximum aerodynamic efficiency (and incidentally also lift) is about 4 times larger than the natural vortex-shedding frequency.

Fig. 12 displays instantaneous vortical structures through Q-criterion iso-surfaces coloured by streamwise velocity. The LES-baseline case (panel a) is characterised by the early separation of the boundary layer and the clear development of Kelvin-Helmholtz vortices along the detached shear layer. These vortices remain predominantly two-dimensional as do all large-scale structures in the vicinity of the airfoil, and are subsumed downstream within the Kármán vortices forming at the top of the wake. The separated region is massive and determines the size of the Kármán vortices that are shed into the wake. The sinuous arrangement of vortices, connected by braids is clearly recognisable and streamwise-cross-stream vortices populate the braid region already one chord distance downstream from the trailing edge.

Actuation drastically reduces the low-speed region above the airfoil and, with it, the width of the wake. Accordingly, lift is enhanced and pressure drag, and along with it total drag, greatly reduced. The SJA-generated spanwise vortices are clearly visible downstream from the jet location as fairly two-dimensional spanwise structures and govern the flow dynamics. They are somewhat more spaced for the LES-$C_l^{\max}$ (panel b) than for the LES-$\eta^{\max}$ case (panel c), on account of the lower actuation frequency of the latter as compared with the former. Kármán vortex-shedding is completely suppressed for LES-$\eta^{\max}$, and highly attenuated for LES-$C_l^{\max}$, for which case smaller-scale spanwise vortices are visible in the wake that become synchronised with the high-frequency vortices induced by the actuator. Two videos showing the vortical structures for the LES-baseline and LES-$\eta^{\max}$ are provided as supplementary data.

5. Conclusions

Following the Synthetic jet Actuation parameters optimisation undertaken by Tousi et al. [1] on the SD7003 airfoil at moderate $Re = 6 \times 10^4$ and post-stall $\alpha = 14°$, we have analysed, using Large Eddy Simulation, the aerodynamic performances and flow properties of optimally actuated scenarios. The original optimisation study, coupled a RANS solver that used the Spalart-Allmaras turbulence model with a Genetic Algorithm specifically devised for maximising either lift or aerodynamic efficiency.

Our Large Eddy Simulation of the baseline case reasonably validated the baseline RANS-SA computation, not without conspicuous discrepancies attributable to the inadequacy of the latter model for the simulation of massively separated flow configurations. However, the two optimal Active Flow Control LES cases, while still producing impressive enhancement of aerodynamic performances, did not align with RANS-SA results as expected. In point of fact, the maximum aerodynamic efficiency case outdoes the other alleged optimum both in terms of aerodynamic efficiency and lift, in this sense constituting an absolute optimum. And not only this, but it also further improves on RANS-SA estimations, with increases from baseline of $\Delta C_l/C_l = 46.7\%$ and $\Delta\eta/\eta = 273.2\%$.

The problem being highly nonlinear, there is no guarantee that the SJA configurations reported here as optimal are indeed absolute optima. They do, however, amply outperform the one SJA study available on the SD7003 airfoil at the same Re and α [2] and produce aerodynamic performances improvements with respect to baseline broadly comparable to those reported in the literature for other airfoils and post-stall flight regimes using alternative optimisation techniques.

A parametric study varying the free-stream turbulent viscosity prescribed at the inlet boundary for actuated simulations with the RANS-SA model reveals that flow topology and aerodynamic performance parameters are highly sensitive, unlike what happens for the baseline case. Turbulent-to-fluid viscosity ratios of around $\tilde{\nu}/\nu \sim 10^{-5}$ enable RANS-SA simulations to better reproduce the actual flow past the actuated airfoil. For these levels of free-stream turbulence, RANS-SA simulation of actuated cases aligned comfortably with LES results, thus proving the convenience of the former for AFC optimisation given their sufficient accuracy and cost-effectiveness. Setting the right amount of free-stream turbulence is however essential, as too low or too large values result in unrealistic flows, possibly due to the poor capabilities of the SA turbulence model for predicting turbulent transition.

The application of optimal (or quasi-optimal) SJA suppresses the boundary layer separation from the upper surface and the shedding of von Kármán vortices in the wake. Actuation-jet-induced spanwise vortices pervade the flow and help maintain quasi-two-dimensionality over a long distance. They also replace the Kelvin-Helmholtz vortices that naturally arise with $f_{\mathrm{KH}} \simeq 15.5$ from a shear layer instability of the separated boundary layer for the baseline case. The jet actuation frequency dominates the spectrum of velocity signals far downstream from the jet location, which indicates that actuation is governing the time- and length-scales of the vortical structures in the flow. Kármán vortices, originally shed with a frequency $f_{\mathrm{vK}} = 0.69$ for the baseline case are no longer present in the wake nor imprint their periodicity on the spectrum of any of the probe signals.

The dependence of the optimum set of SJA parameters on the angle of attack is a matter worth considering, as also is the sensitivity of aerodynamic performances to suboptimal configurations. Some of the parameters, such as actuation frequency, amplitude and, possibly, injection angle, can be adjusted dynamically, while others must be necessarily fixed (slot location and width). For these latter, the sensitivity analysis is particularly relevant, as the one-size-fits-all solution is a must. Also, actuation cannot in practice be continuously distributed along the span, as we have considered here. A discrete number of actuators must instead be distributed along the span with a prescribed spacing, and each could potentially be endowed with a different amplitude, phase or even frequency, such that the set of optimisation parameters can be enlarged unboundedly. These detailed analyses will require extremely costly parametric explorations that are beyond the scope of the present study.

Declaration of competing interest

The authors declare that they have no known competing financial interests or personal relationships that could have appeared to influence the work reported in this paper.

Acknowledgements

This work was supported by the Spanish Government under grants FIS2016-77849-R and PID2020-114043GB-I00 and by the Catalan Government under grant 2017-SGR-00785. Computations were performed in the Red Española de Supercomputación (RES), Spanish supercomputer network, under the grants IM-2019-3-0002 and IM-2020-1-0001. F. M. is a Serra-Húnter fellow.

Appendix A. Supplementary material

Supplementary material related to this article can be found online at https://doi.org/10.1016/j.ast.2022.107679.

References

[1] N.M. Tousi, M. Coma, J.M. Bergada, J. Pons-Prats, F. Mellibovsky, G. Bugeda, Active flow control optimisation on sd7003 airfoil at pre and post-stall angles of attack using synthetic jets, Appl. Math. Model. (2021), https://doi.org/10.1016/j.apm.2021.05.016.
[2] I. Rodriguez, O. Lehmkuhl, R. Borrell, Effects of the actuation on the boundary layer of an airfoil at Reynolds number Re = 60000, Flow Turbul. Combust. 105 (2020) 607–626, https://doi.org/10.1007/s10494-020-00160-y.
[3] L.N. Cattafesta, M. Sheplak, Actuators for active flow control, Annu. Rev. Fluid Mech. 43 (2011) 247–272, https://doi.org/10.1146/annurev-fluid-122109-160634.
[4] L. Wang, F. bao Tian, Numerical simulation of flow over a parallel cantilevered flag in the vicinity of a rigid wall, Phys. Rev. E 99 (2019), https://doi.org/10.1103/physreve.99.053111.
[5] Y.-C. Cho, W. Shyy, Adaptive flow control of low-Reynolds number aerodynamics using dielectric barrier discharge actuator, Prog. Aerosp. Sci. 47 (2011) 495–521, https://doi.org/10.1016/j.paerosci.2011.06.005.
[6] S. Foshat, Numerical investigation of the effects of plasma actuator on separated laminar flows past an incident plate under ground effect, Aerosp. Sci. Technol. 98 (2020) 105646, https://doi.org/10.1016/j.ast.2019.105646.
[7] N. Benard, E. Moreau, Electrical and mechanical characteristics of surface AC dielectric barrier discharge plasma actuators applied to airflow control, Exp. Fluids 55 (2014), https://doi.org/10.1007/s00348-014-1846-x.
[8] N. Benard, J. Pons-Prats, J. Periaux, G. Bugeda, P. Braud, J. Bonnet, E. Moreau, Turbulent separated shear flow control by surface plasma actuator: experimental optimization by genetic algorithm approach, Exp. Fluids 57 (2016), https://doi.org/10.1007/s00348-015-2107-3.
[9] M.G. De Giorgi, V. Motta, A. Suma, Influence of actuation parameters of multi-dbd plasma actuators on the static and dynamic behaviour of an airfoil in unsteady flow, Aerosp. Sci. Technol. 96 (2020) 105587.
[10] A. Glezer, M. Amitay, Synthetic jets, Annu. Rev. Fluid Mech. 34 (2002) 503–529.
[11] C. Rumsey, T. Gatski, W. Sellers, V. Vatsa, S. Viken, Summary of the 2004 cfd validation workshop on synthetic jets and turbulent separation control, in: 2nd AIAA Flow Control Conference, 2004, p. 2217.
[12] I. Wygnanski, The variables affecting the control of separation by periodic excitation, in: 2nd AIAA Flow Control Conference, 2004, p. 2505.
[13] N. Findanis, N. Ahmed, The interaction of an asymmetrical localised synthetic jet on a side-supported sphere, J. Fluids Struct. 24 (2008) 1006–1020, https://doi.org/10.1016/j.jfluidstructs.2008.02.002.
[14] L. Zhiyong, L. Zhenbing, L. Qiang, Z. Yan, Modulation of driving signals in flow control over an airfoil with synthetic jet, Chin. J. Aeronaut. 33 (2020) 3138–3148.
[15] M. De Giorgi, C. De Luca, A. Ficarella, F. Marra, Comparison between synthetic jets and continuous jets for active flow control: application on a NACA 0015 and a compressor stator cascade, Aerosp. Sci. Technol. 43 (2015) 256–280, https://doi.org/10.1016/j.ast.2015.03.004.
[16] S. Traficante, M. De Giorgi, A. Ficarella, Flow separation control on a compressor-stator cascade using plasma actuators and synthetic and continuous jets, J. Aerosp. Eng. 29 (2016) 04015056.
[17] M.G. De Giorgi, S. Traficante, C. De Luca, D. Bello, A. Ficarella, Active flow control techniques on a stator compressor cascade: a comparison between synthetic jet and plasma actuators, in: Turbo Expo: Power for Land, Sea, and Air, vol. 44748, American Society of Mechanical Engineers, 2012, pp. 439–450.
[18] H. Zhang, S. Chen, Y. Gong, S. Wang, A comparison of different unsteady flow control techniques in a highly loaded compressor cascade, Proc. Inst. Mech. Eng., G J. Aerosp. Eng. 233 (2019) 2051–2065.
[19] M. Amitay, D.R. Smith, V. Kibens, D.E. Parekh, A. Glezer, Aerodynamic flow control over an unconventional airfoil using synthetic jet actuators, AIAA J. 39 (2001) 361–370, https://doi.org/10.2514/3.14740.
[20] M. Amitay, A. Glezer, Role of actuation frequency in controlled flow reattachment over a stalled airfoil, AIAA J. 40 (2002) 209–216, https://doi.org/10.2514/3.15052.
[21] J. Gilarranz, L. Traub, O. Rediniotis, A new class of synthetic jet actuators—part i: design, fabrication and bench top characterization, J. Fluids Eng. 127 (2005) 367–376, https://doi.org/10.1115/1.1839931.
[22] D. You, P. Moin, Active control of flow separation over an airfoil using synthetic jets, J. Fluids Struct. 24 (2008) 1349–1357, https://doi.org/10.1016/j.jfluidstructs.2008.06.017.
[23] A. Tuck, J. Soria, Separation control on a NACA 0015 airfoil using a 2d micro ZNMF jet, Aircr. Eng. Aerosp. Technol. 80 (2008) 175–180, https://doi.org/10.1108/00022660810859391.
[24] V. Kitsios, L. Cordier, J.-P. Bonnet, A. Ooi, J. Soria, On the coherent structures and stability properties of a leading-edge separated aerofoil with turbulent recirculation, J. Fluid Mech. 683 (2011) 395–416, https://doi.org/10.1017/jfm.2011.285.
[25] N. Buchmann, C. Atkinson, J. Soria, Influence of ZNMF jet flow control on the spatio-temporal flow structure over a NACA-0015 airfoil, Exp. Fluids 54 (2013), https://doi.org/10.1007/s00348-013-1485-7.
[26] P. Itsariyapinyo, R.N. Sharma, Large Eddy simulation of a naca0015 circulation control airfoil using synthetic jets, Aerosp. Sci. Technol. 82 (2018) 545–556.
[27] S.H. Kim, C. Kim, Separation control on NACA23012 using synthetic jet, Aerosp. Sci. Technol. 13 (2009) 172–182, https://doi.org/10.1016/j.ast.2008.11.001.
[28] H.E. Monir, M. Tadjfar, A. Bakhtian, Tangential synthetic jets for separation control, J. Fluids Struct. 45 (2014) 50–65, https://doi.org/10.1016/j.jfluidstructs.2013.11.011.
[29] S.D. Goodfellow, S. Yarusevych, P.E. Sullivan, Momentum coefficient as a parameter for aerodynamic flow control with synthetic jets, AIAA J. 51 (2013) 623–631, https://doi.org/10.2514/1.j051935.
[30] M.A. Feero, S.D. Goodfellow, P. Lavoie, P.E. Sullivan, Flow reattachment using synthetic jet actuation on a low-Reynolds-number airfoil, AIAA J. 53 (2015) 2005–2014, https://doi.org/10.2514/1.j053605.
[31] M.A. Feero, P. Lavoie, P.E. Sullivan, Influence of synthetic jet location on active control of an airfoil at low Reynolds number, Exp. Fluids 58 (2017), https://doi.org/10.1007/s00348-017-2387-x.
[32] W. Zhang, R. Samtaney, A direct numerical simulation investigation of the synthetic jet frequency effects on separation control of low-Re flow past an airfoil, Phys. Fluids 27 (2015) 055101, https://doi.org/10.1063/1.4919599.
[33] M.S. Selig, J.F. Donovan, D.B. Fraser, Airfoils at low speeds, HA Stokely, 1989.
[34] M. Selig, J. Guglielmo, A. Broeren, P. Giguere, Summary of low-speed airfoil data summary of low-speed airfoil data, Tech. Rep., University of Illinois, 1995.
[35] M. Breuer, Effect of inflow turbulence on an airfoil flow with laminar separation bubble: an les study, Flow Turbul. Combust. 101 (2018) 433–456.
[36] S. Qin, M. Koochesfahani, F. Jaberi, Large Eddy simulations of unsteady flows over a stationary airfoil, Comput. Fluids 161 (2018) 155–170.
[37] R. Duvigneau, M. Visonneau, Simulation and optimization of stall control for an airfoil with a synthetic jet, Aerosp. Sci. Technol. 10 (2006) 279–287, https://doi.org/10.1016/j.ast.2006.01.002.
[38] V.J. Torczon, Multidirectional search: a direct search algorithm for parallel machines, Ph.D. thesis, Rice University, 1989, https://hdl.handle.net/1911/16304.
[39] R. Duvigneau, A. Hay, M. Visonneau, Optimal location of a synthetic jet on an airfoil for stall control, J. Fluids Eng. 129 (2007) 825–833, https://doi.org/10.1115/1.2742729.
[40] D. Kamari, M. Tadjfar, A. Madadi, Optimization of SD7003 airfoil performance using TBL and CBL at low Reynolds numbers, Aerosp. Sci. Technol. 79 (2018) 199–211.
[41] M. Tadjfar, D. Kamari, Optimization of flow control parameters over SD7003 airfoil with synthetic jet actuator, J. Fluids Eng. 142 (2020), https://doi.org/10.1115/1.4044985.

[42] M. Galbraith, M. Visbal, Implicit large Eddy simulation of low Reynolds number flow past the SD7003 airfoil, in: 46th AIAA Aerospace Sciences Meeting and Exhibit, American Institute of Aeronautics and Astronautics, 2008, p. 225.

[43] S. Burgmann, W. Schröder, Investigation of the vortex induced unsteadiness of a separation bubble via time-resolved and scanning piv measurements, Exp. Fluids 45 (2008) 675.

[44] W. Zhang, R. Hain, C.J. Kähler, Scanning piv investigation of the laminar separation bubble on a sd7003 airfoil, Exp. Fluids 45 (2008) 725–743.

[45] P. Catalano, R. Tognaccini, Turbulence modeling for low-Reynolds-number flows, AIAA J. 48 (2010) 1673–1685, https://doi.org/10.2514/1.j050067.

[46] P. Catalano, R. Tognaccini, Rans analysis of the low-Reynolds number flow around the sd7003 airfoil, Aerosp. Sci. Technol. 15 (2011) 615–626.

[47] P. Spalart, S. Allmaras, A one-equation turbulence model for aerodynamic flows, in: 30th Aerospace Sciences Meeting and Exhibit, 1992, p. 439.

[48] F. Nicoud, F. Ducros, Subgrid-scale stress modelling based on the square of the velocity gradient tensor, Flow Turbul. Combust. 62 (1999) 183–200.

[49] O. Lehmkuhl, I. Rodríguez, A. Baez, A. Oliva, C. Pérez-Segarra, On the large-Eddy simulations for the flow around aerodynamic profiles using unstructured grids, Comput. Fluids 84 (2013) 176–189.

[50] A.K. Shukla, A. Dewan, Flow and thermal characteristics of jet impingement on a flat plate for small nozzle to plate spacing using les, Int. J. Therm. Sci. 145 (2019) 106005.

[51] P. Catalano, R. Tognaccini, Influence of free-stream turbulence on simulations of laminar separation bubbles, in: 47th AIAA Aerospace Sciences Meeting Including the New Horizons Forum and Aerospace Exposition, 2009, p. 1471.

[52] C.J. Greenshields, Openfoam user guide version 6, The OpenFOAM Foundation, 2018, p. 237.

[53] R.I. Issa, Solution of the implicitly discretised fluid flow equations by operator-splitting, J. Comput. Phys. 62 (1986) 40–65.

[54] U. Piomelli, J.R. Chasnov, Large-Eddy simulations: theory and applications, in: Turbulence and Transition Modelling, Springer, 1996, pp. 269–336.

[55] S.B. Pope, Ten questions concerning the large-Eddy simulation of turbulent flows, New J. Phys. 6 (2004) 35.

[56] C. Geuzaine, J.-F. Remacle Gmsh, A 3-d finite element mesh generator with built-in pre-and post-processing facilities, Int. J. Numer. Methods Eng. 79 (2009) 1309–1331.

[57] K. Deb, A. Pratap, S. Agarwal, T. Meyarivan, A fast and elitist multiobjective genetic algorithm: NSGA-II, IEEE Trans. Evol. Comput. 6 (2002) 182–197, https://doi.org/10.1109/4235.996017.

[58] K. Deb, R.B. Agrawal, Simulated binary crossover for continuous search space, Complex Syst. 9 (1995) 115–148.

[59] K. Deb, Multi-Objective Optimization Using Evolutionary Algorithms, vol. 16, John Wiley & Sons, Chichester, UK, 2001.